The mammalian SKI complex is a broad-spectrum antiviral drug target that upregulates cellular cholesterol to inhibit viral replication

Short Title: Drug targeting the SKI complex increases cellular cholesterol

Stuart Weston[a], Lauren Baracco[a], Louis Taylor[a], Alison Scott[b,c], Gaurav Kumar[d], Paul Shapiro[d], Alexander D. MacKerell Jr. [d], and Matthew B. Frieman[a*]

[a] Center for Pathogen Research, Department of Microbiology and Immunology, University of Maryland School of Medicine, Baltimore, MD, 21201

[b] Department of Microbial Pathogenesis, University of Maryland School of Dentistry, Baltimore, MD, 21201

[c] Department of Microbiology and Immunology, University of Maryland School of Dentistry, Baltimore, MD, 21201

[d] Department of Pharmaceutical Sciences, University of Maryland School of Pharmacy, Baltimore, MD, 20201

* Corresponding author: MFrieman@som.umaryland.edu

Abstract

There is a need for the development of broad-spectrum antiviral compounds that can act as first line therapeutic countermeasures to emerging viral infections. Host-directed approaches present a promising avenue of development and carry the benefit of mitigating risks of viral escape mutants. We have previously found the SKI (super killer) complex to be a broad-spectrum, host-target with our lead compound ("UMB18") showing activity against influenza A virus, coronaviruses, and filoviruses. The SKI complex is a cytosolic RNA helicase and we previously found that UMB18 inhibited viral RNA production but did not further define the mechanism. Here, we demonstrate that UMB18 directly binds to SKIC8 of the SKI complex and through transcriptomic analysis of UMB18 treated A549 cells revealed an upregulation of genes in the mevalonate pathway which drives cholesterol synthesis. Further investigation validated the genetic upregulation and confirmed an increase in total cellular cholesterol. This upregulation was dependent on the sterol regulatory element binding proteins (SREBPs) and their regulator SCAP, the major regulators for cholesterol and fatty acid synthesis. Depletion of the SREBPs or SCAP with siRNA, or extraction of cholesterol with methyl β-cyclodextrin attenuated UMB18 antiviral activity, emphasizing the role of increased cholesterol synthesis in this mechanism of action. Our findings further define the antiviral mechanism of a developmental host-directed therapeutic approach with broad applicability against emerging viral pathogens.

Author Summary

The COVID-19 pandemic has underscored the urgent need for effective countermeasures to novel and emerging viral pathogens. Our research presented here builds upon our previously published data on an experimental novel antiviral compound termed UMB18. We have found this compound capable of inhibiting replication of influenza A virus, coronaviruses and the filoviruses Marburg and Ebola virus, but did not fully define a mechanism of action. In this work, we demonstrate that UMB18 exerts antiviral activity by modulating cellular cholesterol levels. By targeting the SKI complex, UMB18 triggers an increase in endogenous cellular cholesterol which disrupts the fine balance viruses rely on for efficient infection. We demonstrate that this mechanism inhibits replication of SARS-CoV-2, revealing a previously undescribed host-directed strategy for antiviral intervention. These findings highlight UMB18's potential as a broad-spectrum antiviral agent and pave the way for further research into its mechanism and therapeutic applications, offering a promising avenue for development of antiviral countermeasures to current, novel and emerging pathogens.

Introduction

The coronavirus disease-2019 (COVID-19) pandemic caused by severe acute respiratory syndrome coronavirus-2 (SARS-CoV-2) has highlighted the lack of broadly acting therapeutics to treat coronaviruses and other emerging pathogens. These types of chemicals could serve as first-line countermeasures, filling a crucial gap before specific measures can be developed. Addressing this need, our research is focused on a host-directed approach of targeting the SKI (super killer) complex (1).

As opposed to direct acting antivirals, host-directed therapeutics have a significantly lower risk for the emergence of viral escape mutants, but such strategies come with a greater risk of side effects. It is therefore essential to understand the mechanism of action for any such approach.

Comprised of SKIC2, SKIC3, and SKIC8 (formerly SKIV2L, TTC37, and WDR61, respectively) the SKI complex acts as a cofactor to the cytosolic RNA exosome to facilitate 3' to 5' RNA degradation (2–4). SKIC2 is a member of the DExD/H helicase family, while SKIC3 and SKIC8 have structural and regulatory functions (5). The complex was first defined in yeast where it was implicated in resistance to the "super killer" toxin of a yeast double stranded RNA virus, hence the naming convention of SKI (6,7). Our previous study demonstrated that siRNA depletion of the SKI complex inhibited replication of influenza A virus (IAV) and Middle East respiratory syndrome coronavirus (MERS-CoV). We proceeded to use *in silico* modeling to predict chemicals that could hypothetically bind SKIC8 and potentially disrupt the proviral activity of the

79 SKI complex. We demonstrated that our lead compound, termed UMB18, inhibited all of
80 IAV, MERS-CoV, SARS-CoV, SARS-CoV-2, and the filoviruses Ebola virus and Marburg
81 virus. Then, using single cycle IAV infections, we determined that UMB18 did not impact
82 virus entry to cells, but potently inhibited RNA and subsequent protein production. Thus,
83 we defined UMB18 as a host-directed antiviral, targeting post-entry steps prior to RNA
84 production, with broad-spectrum activity (1).
85
86 In the present study, UMB18 was found to bind SKIC8 demonstrating specificity of our
87 previously predicted binding. We subsequently found transcriptomic upregulation of
88 genes involved in cholesterol synthesis and concomitant increases in total cholesterol
89 following UMB18 treatment of cells. Cholesterol can be obtained from external sources
90 through low-density lipoprotein (LDL) receptors or endogenously synthesized through
91 the mevalonate pathway (8–10). Sterol regulatory element binding proteins (SREBPs)
92 are master transcriptional regulators of cholesterol and fatty acid synthesis (11).
93 SREBPs comprise three isoforms, SREBP1a, SREBP1c, and SREBP2, expressed from
94 two genes *Srebf1* and *Srebf2* (12,13). Each of the SREBP proteins are regulated by
95 SREBP-cleavage activating protein (SCAP) (14,15). We found that depletion of *Scap,*
96 *Srebf1* or *Srebf2* reduced UMB18-mediated increases in mevalonate pathway genes.
97 Notably, UMB18 antiviral activity against SARS-CoV-2 was significantly reduced with
98 either depletion of the *Scap* or *Srebf* genes or extraction of cholesterol with methyl-β
99 cyclodextrin. These results underscore the importance of increased total cellular
100 cholesterol in the mechanism of action for UMB18 as an antiviral compound.

101 Overall, the work presented here demonstrates the promise of UMB18 as a broad-
102 spectrum, host-directed antiviral compound and elucidates its mechanism of action
103 through upregulation of cellular cholesterol synthesis by targeting the SKI complex.
104

105 Results

106 **UMB18 binds SKIC8 and upregulates genes involved in cholesterol synthesis.**
107 We previously described the broad-spectrum antiviral activity of the SKI-targeted
108 compound UMB18 (1) and now aimed to identify its mechanism of action. The
109 compound was developed using *in silico* modeling and was predicted to bind to SKIC8
110 (formerly WDR61). The genes of the SKI complex are required for the antiviral activity of
111 UMB18, suggesting specificity but we did not demonstrate that UMB18 directly binds to
112 the predicted target SKIC8 (1). We therefore expressed and purified SKIC8 from
113 bacterial cells and analyzed UMB18 binding by surface plasmon resonance (SPR). The
114 fast association and dissociation rate constants observed at various compound
115 concentrations indicated binding to the SKIC8 target with a relatively low binding affinity,
116 KD = 81 μM (Fig. 1A). These data suggest that UMB18 is indeed directly binding to
117 SKIC8.
118

119 Having determined that our compound is specific to the *in silico* predicted target, we
120 next utilized RNA transcriptomics to investigate the changes that UMB18 binding SKIC8
121 can cause, both in uninfected or SARS-CoV-2 infected cells. This provided an unbiased
122 approach to investigate potential mechanisms of antiviral activity. A549 cells (human
123 lung alveolar adenocarcinoma cells) overexpressing human angiotensin converting

124 enzyme 2 (A549-ACE2) to allow for productive SARS-CoV-2 infection were used for the
125 transcriptomic analysis and four conditions were analyzed: 1) 10 μM UMB18 treatment,
126 2) 0.1% DMSO treatment (carrier for UMB18), 3) 10 μM UMB18 with SARS-CoV-2
127 infection or 4) 0.1% DMSO with SARS-CoV-2 infection. We previously found 10 μM to
128 be inhibitory to viral replication with no cytotoxicity (see (1) and also Fig. 6F). All
129 infections were at multiplicity of infection (MOI) 0.1, performed across two experiments,
130 with either 24-hour (h) and 48h or just a 24h of infection and treatment. In uninfected
131 cells, the most prominently differentially expressed genes caused by UMB18 treatment
132 compared to DMSO were in the mevalonate pathway, associated with cholesterol
133 biosynthesis (Fig. 1B-D). As expected, SARS-CoV-2 infection had minimal impact on
134 the genes that were upregulated with UMB18 treatment compared to DMSO, with the
135 majority of significantly upregulated genes occurring in all conditions (Fig. 1E). Eight
136 genes (MSMO1, IDI1, FDFT1, HMGCS1, DHCR24, LSS, FDPS, MVD) were
137 significantly upregulated at both time points and both infection conditions, while five
138 genes (SQLE, ACAT2, EBP, TM7SF2, DHCR7) were upregulated by UMB18 treatment
139 at 24h and 48h infection as well as at the 24h but not the 48h time point in uninfected
140 cells. MVK and HSD17B7 were upregulated at 24h in infected and uninfected cells,
141 while CYP51A1 and NSDHL were upregulated in the context of infection at 24h and 48h
142 but not in uninfected cells. HMGCR was upregulated at 24h and 48h in uninfected cells
143 and at 48h in infected cells (Fig. 1E). These studies used bulk RNA sequencing with a
144 low MOI of SARS-CoV-2 and 10 μM UMB18 treatment causes a roughly 90% inhibition
145 of infection. As expected, low levels of SARS-CoV-2 replication are occurring in the
146 treated cells (for example see Fig. 6F), therefore we did not expect to see major

147 differences with infection. This data set was included for completeness and as a
148 comparator to the uninfected cells. The analysis demonstrated upregulation of genes
149 involved in the mevalonate pathway after treatment with UMB18 which may have a role
150 in antiviral activity.
151
152 **UMB18 treatment increases cellular cholesterol levels.**
153 The upregulation of the mevalonate pathway through the transcriptomic analysis
154 suggested that cholesterol synthesis may be affected by UMB18. We validated the
155 results of the transcriptomic analysis using qRT-PCR with primers targeting a subset of
156 the genes in the mevalonate pathway. Identical to the previous experiment, A549-ACE2
157 cells were treated with 10 μM UMB18 or 0.1% DMSO as the vehicle control for 24 or
158 48h. Additionally, A549 cells not expressing ACE2 were subject to the same treatments
159 to further validate the results and ensure that ACE2 overexpression was not impacting
160 the transcriptional changes. Seven genes for enzymes involved in various stages of the
161 mevalonate pathway were analyzed to get a broad view of transcriptional changes
162 (pathway schematic in Fig. 2A, yellow boxes are selected genes for analysis). Relative
163 to DMSO treatment, UMB18 caused a significant increase in expression of genes in the
164 mevalonate pathway, ranging from approximately 2- to 5-fold. In the A549-ACE2 cells
165 (Fig. 2B), induction of the selected genes peaked at 24h and then declined by 48h. With
166 48h treatment, the genes were still more highly expressed than DMSO control cells but
167 lacked the statistically significant differences seen at 24h (Fig. 2B). We suspect this may
168 be a result of other feedback regulatory loops in the pathway or due to degradation of
169 UMB18 in the media as it was not replenished through the time course. In A549 cells,

170 UMB18 treatment caused an increase in expression of each of the genes that similarly
171 peaked at 24h and declined at 48h. These changes remained statistically significant
172 compared to DMSO controls at 48h (Fig. 2C). The magnitude of change between the
173 two cell lines was largely similar. Overall, these qRT-PCR data suggest that UMB18
174 caused an increase in genes that regulate cholesterol synthesis through the mevalonate
175 pathway and that the expression of ACE2, which allows for infection by SARS-CoV-2,
176 does not significantly alter the magnitude of change.
177
178 We next investigated whether total cellular cholesterol was increased in the cells, since
179 we identified an increase in the expression of genes involved in the mevalonate
180 pathway with UMB18 treatment. To this end, we utilized silver-assisted laser desorption
181 ionization mass spectrometry imaging (Ag-LDI MSI), a highly sensitive method of
182 detecting total cellular cholesterol. A549-ACE2 cell culture monolayers treated with
183 UMB18 showed a higher intensity of cholesterol signal compared to DMSO-treated
184 cells. Cholesterol was detected and visualized in the monolayers as the ion *m/z* 493.260
185 +/- 2.2 mDa ([cholesterol+Ag107]+) ion (Fig. 2D) and the silver isotopologue ion
186 [cholesterol+Ag109]+ data agreed. Treatment with UMB18 resulted in a significant
187 increase in relative cholesterol abundance, showing a nearly 2-fold increase in pixel
188 intensities. Further, a receiver-operator characteristic analysis showed an area-under-
189 the-curve value of 0.804 for cholesterol in UMB18 treated cells, making cholesterol
190 abundance a strong discriminator over DMSO-treated cells. These data demonstrate
191 that UMB18 treatment of A549-ACE2 cells results in significantly and discriminatorily
192 higher amounts of cholesterol compared to control.

193

194 **UMB18 increases cellular cholesterol and exerts antiviral activity in serum**

195 **containing media.**

196 Experiments to investigate changes caused by UMB18 treatment were performed in

197 serum supplemented media and therefore have exogenous cholesterol available. Cells

198 can endocytose cholesterol through the LDL-receptor and activate a negative feedback

199 loop to inhibit the mevalonate pathway. It therefore appeared UMB18 may activate this

200 metabolic pathway even in the presence of exogenous cholesterol. To further analyze

201 the system, we treated A549-ACE2 cells with 10 μM UMB18 or 0.1% DMSO in serum-

202 containing or serum-free media, isolated RNA at 24h, and performed qRT-PCR for a

203 subset of the mevalonate pathway genes. In serum-containing media, UMB18 treatment

204 resulted in a similar significantly increased gene expression for the mevalonate pathway

205 genes HMGCS1, MVD and MSMO1 (Fig. 3A-C). In serum-free media, there was an

206 upregulation of these three genes, in both DMSO and UMB18 containing media, with no

207 significant differences between the two. Serum-free media caused a statistically

208 significantly larger increase in expression compared to UMB18 in serum-containing

209 media in all cases (Fig. 3A-C). These data show that in the absence of exogenous

210 cholesterol from serum, the mevalonate pathway was activated as expected and, in that

211 context, UMB18 did not further enhance the level of mevalonate pathway associated

212 gene transcription. However, in media containing serum, UMB18 did cause a

213 statistically significant increase in genes involved in the mevalonate pathway.

214

215 We hypothesized that this increase in cholesterol synthesis caused by UMB18 plays a
216 role in antiviral activity against SARS-CoV-2. We therefore infected A549-ACE2 cells
217 with SARS-CoV-2 at MOI 0.1 in serum-containing or serum-free media and treated with
218 10 μM UMB18 or 0.1% DMSO for 24h prior to supernatant collection and quantitation of
219 virus by plaque assay. UMB18 was equally effective at inhibiting viral replication
220 regardless of the presence of serum (Fig. 3D). In serum-free media containing DMSO,
221 there is a small (3x), but statistically significant drop in viral titer compared to serum-
222 containing media, suggesting that the increased expression of mevalonate pathway
223 genes may have an impact on viral replication (Fig. 3D). The inhibition is not as potent
224 as UMB18 treatment, and we hypothesize this may be a temporal effect with UMB18
225 causing a more rapid increase in expression of the genes that have activity and inhibit
226 early stages of the viral life cycle.
227
228 **SCAP and SREBP are required for UMB18-induced increases in mevalonate**
229 **pathway genes.**
230 Our data suggest that UMB18 binds to the SKI complex and consequently increases
231 expression of genes in the mevalonate pathway leading to an increase in total cellular
232 cholesterol. We set out to determine what cellular pathways the SKI complex might be
233 interacting with to mediate this effect. First, we looked at the mammalian target of
234 rapamycin (mTOR) complex because of published findings that demonstrated a loss of
235 SKIC2 activity was connected to an increase in mTORC1 signaling (16). The mTOR
236 complex is a master regulator of numerous aspects of cellular metabolism and it can
237 regulate activation of the sterol regulatory element binding proteins (SREBPs) which

238 promote expression of the mevalonate genes. We analyzed the ribosomal protein S6
239 kinase 1 (S6K1) which is phosphorylated when the mTOR pathway is activated. Using
240 treatment with epidermal growth factor (EGF), a known activator of the mTOR pathway,
241 we were able to detect phospho-S6K1 (pS6K1), demonstrating that our cells showed a
242 canonical marker for mTOR signaling (Fig. 4A). We proceeded to treat cells with UMB18
243 for various time points for analysis (Fig. 4B-C). None of these treatments showed any
244 significant changes to phospho-S6K1, suggesting that UMB18 did not cause a
245 detectable activation of mTOR, at least based on phosphorylation of S6K1.
246
247 Since UMB18 did not show any clear activation of mTOR, we next investigated the
248 master regulators of cholesterol and fatty acid synthesis, the SREBPs. Two genes,
249 *Srebf1* and *Srebf2,* produce three proteins, SREBP-1a, SREBP-1c, and SREBP2 and
250 all of these are regulated by SREBP cleavage activating protein (SCAP), encoded by
251 the *Scap* gene (11,13,14,17). Transfection of siRNAs targeting each of these three
252 genes into A549-ACE2 cells was used for knockdown studies. At 72h post siRNA
253 transfection, cells were treated with DMSO or UMB18 for 24h and RNA collected to
254 perform qRT-PCR for each of the siRNA targets and three mevalonate pathway genes
255 (Fig. 5). We hypothesized that if UMB18 was activating mevalonate pathway gene
256 expression through the canonical route, reduced expression of SCAP or SREBPs would
257 reduce the impact of this treatment.
258
259 SCAP is the master regulator for activation of the SREBPs. We targeted SCAP with two
260 different siRNA sequences and both caused a significantly decreased expression of

261 *Scap* relative to scrambled siRNA (siScr), with sequence 2 being more potent that
262 sequence 1 (Fig. 5A). There was no significant impact of UMB18 treatment upon
263 expression of *Scap* in any context (Fig. 5A). In siScr transfected cells treated with
264 UMB18, there was a significant increase in expression of *MVD*, *FDPS* and *MSMO1*
265 compared to DMSO treated cells (Fig. 5B-D, right most pairs). Each gene had 4 times
266 the expression level based on the qRT-PCR data, matching previous results (Fig. 2 and
267 3). In the context of *Scap* siRNA there was no significant difference between UMB18
268 and DMSO treated cells for *MVD* and *FDPS* gene expression (Fig. 5B and C), but there
269 were significant changes for *MSMO1* ($p = 0.0305$ and 0.0158 for siRNA sequence 1 and
270 2; Fig 5D). However, the relative fold change was significantly lower than that caused by
271 UMB18 in siScr transfected cells (both $p < 0.0001$). These data all suggest that UMB18
272 did not impact the expression of *Scap*, but when expression of this gene was reduced
273 through siRNA-mediated knockdown there was a significantly reduced impact of UMB18
274 on the mevalonate pathway genes. This suggests that UMB18 treatment activates
275 expression of these genes through a canonical pathway mediated by SCAP.
276
277 To further validate that UMB18 is impacting this canonical signaling pathway, we also
278 targeted the *Srebf* genes with siRNA. *Srebf2* was knocked down with 2 separate siRNA
279 sequences similarly to *Scap* and both caused a significant decrease in expression.
280 Sequence 1 was more potent than 2, however both caused a significant decrease in
281 gene expression (Fig. 5E). UMB18 did have some impact on *Srebf2*, unlike the results
282 for *Scap*, but that could be attributed to the increase in mevalonate pathway genes
283 since *Srebf2* is in a positive feedback loop. In the context of siScr there was a mild

284 increase in expression, and the p value was calculated to 0.0504. Similarly, in the
285 context of siRNA sequence 2, there was significantly less reduction in *Srebf2*
286 expression cause by UMB18 treatment, with a p value of 0.0035 between UMB18 and
287 DMSO conditions. However, compared to siScr transfection and DMSO treatment, the
288 UMB18 treated cells still had an approximate 2-fold decrease in expression, suggesting
289 any impact from UMB18 does not outweigh the inhibition from the siRNA. For each of
290 the mevalonate pathway genes, once again, UMB18 caused a significant increase in
291 expression compared to DMSO within the control condition of siScr transfection (Fig 5F-
292 H, right most pairs). Loss of *Srebf2* appeared to have less impact on the UMB18-
293 mediated changes than *Scap* with significant changes observed in both siRNA
294 transfection conditions for *MVD* (Fig 5F), and the context of siRNA sequence 2 for
295 *MSMO1* (Fig. 5H). However, the changes in *FDPS* were not significant between UMB18
296 and DMSO with either siRNA sequence (Fig 5H). and for sequence 1 for *MSMO1*
297 expression (Fig 5H, left most pair). These data suggest that reduced *Srebf2* expression
298 through siRNA reduced the impact UMB18 had on altering expression of these three
299 mevalonate pathway genes, however, the targeting of *Scap* with siRNA appeared to
300 cause a more potent inhibition.
301
302 Finally, to complete this investigation of the SCAP/SREBP pathway, *Srebf1* was
303 targeted with siRNA, with 3 different siRNA sequences. While all of the sequences
304 caused approximately a 4x or greater decrease in expression, these data did not reach
305 statistical significance, with the exception of siRNA sequence 2 compared to siScr in the
306 context of DMSO treatment (Fig 5I). UMB18 did not significantly impact expression of

307 *Srebf1* (Fig. 5I). As for other experiments, UMB18, in the context of siScr transfection,
308 caused a significant increase in expression of *MVD*, *FDPS* and *MSMO1* compared to
309 DMSO treatment (Fig. 5J-L, right most pairs). Even though the three siRNA sequences
310 did not consistently cause a statistically significant decrease in expression, all of them
311 showed varying levels of decrease for UMB18 impact on gene expression. For *MVD*,
312 siRNA sequence 2 and 3 both had a significantly reduced fold change for UMB18
313 treatment (Fig 5J, $p = 0.0006$ and 0.0350). For *FDPS*, all three sequences had
314 significantly reduced fold changes (Fig. 5K) and for siRNA sequence 2 there was a
315 significant reduction in UMB18 induced changes to *MSMO1* expression (Fig. 5L). These
316 data suggest that even though these siRNA sequences did not cause statistically
317 significant reduction in *Srebf1* expression, all of them caused significant inhibition of
318 UMB18 induced changes.
319
320 Overall, the data in Fig. 5 demonstrate that UMB18 caused an increase in expression of
321 genes in the mevalonate pathway (represented by *MVD*, *FDPS* and *MSMO1*) without
322 causing major changes to *Scap*, nor the *Srebf* genes. However, when the
323 SCAP/SREBP axis is disrupted by siRNA treatment, there were significant reductions to
324 the impact from UMB18 on expression of mevalonate pathway genes. Our results
325 demonstrate that UMB18 directly binds to the SKI complex (Fig. 1A) and causes genetic
326 activation of the mevalonate pathway (Fig. 2, 3 and 5) which relies on the canonical
327 activation of SCAP/SREBPs.
328
329 **Increased cellular cholesterol is required for UMB18-mediated antiviral activity.**

330 We have found that UMB18 caused an increase in mevalonate pathway gene
331 expression and that the canonical signaling pathway mediated by SCAP and SREBPs is
332 involved. This transcriptional response increased total cellular cholesterol, leading to the
333 question of whether the increase in cholesterol is important for antiviral activity. To
334 investigate this, we again used siRNA to target *Scap* and the *Srebf* genes and treated
335 cells with UMB18 while also infecting with SARS-CoV-2. A549-ACE2 cells were plated
336 and transfected for 72h. Cells were then infected with SARS-CoV-2 at MOI 0.1 and
337 treated with 10 μM UMB18 or 0.1% DMSO for 24h. Supernatant were collected, and
338 viral titer determined by plaque assay on VeroE6 cells expressing transmembrane
339 protease serine 2 (TMPRSS2). With scrambled siRNA there was an approximate 10-
340 fold drop in viral titer (Fig. 6A-C), similar to the effects we previously published (1).
341 However, when *Scap* was knocked down by siRNA, UMB18 lowered viral titer by 4.36-
342 and 2.92-fold compared to DMSO and was not significantly different (Fig. 6A and C).
343 These data suggest the reduction in *Scap* expression caused by siRNA reduced the
344 antiviral activity of UMB18, making it not statistically significant compared to DMSO.
345 When *Srebf2* was targeted by siRNA sequence 1 there was only a 2.05-fold difference
346 between UMB18 and DMSO (but this was statistically significant), while sequence 2 had
347 less impact with a 7.52-fold difference. These differences are in alignment with the
348 potency of the siRNA sequences for knockdown of *Srebf2*, with sequence 2 being less
349 potent (Fig. 5E) and causing less impact to UMB18 antiviral activity. For Srebf*1*
350 knockdown down, UMB18 lowered viral titer by only between 1.23- to 2.04-fold,
351 compared to DMSO (Fig. 6C), suggested even great loss of inhibition. In all cases, viral
352 titer inhibition due to UMB18 is attenuated by loss of SCAP and SREBPs, with varying

353 degrees of significance. Since the loss of these genes causes a decrease in
354 mevalonate pathway gene expression induced by UMB18 (Fig. 5), these data
355 collectively suggest that increased cellular cholesterol plays a role in UMB18-mediated
356 antiviral activity.
357
358 We also investigated the effects of methyl-β cyclodextrin (MβCD), a chemical that
359 extracts cholesterol from cells, to see if this would disrupt UMB18 antiviral activity.
360 Initially, A549-ACE2 cells were treated with a range of concentrations between 39 and
361 5000 µg/ml to investigate toxicity. The higher concentrations resulted in cell death based
362 on automated counting of nuclei in a 96-well plate format (Fig. 6D). At 625 µg/ml and
363 lower, there were no signs of toxicity. A549-ACE2 cells were then infected with SARS-
364 CoV-2 at MOI 3 and treated with MβCD at non-cytotoxic concentrations. At 24 hours
365 post-infection cells were fixed and immunofluorescent labeled for the viral N protein and
366 high content imaged to determine the percentage infection. Fig. 6E demonstrates that
367 MβCD has some level of antiviral activity with 625, 312.5, and 156.25 µg/ml causing
368 roughly 30-40% fewer infected cells compared to DMSO-treated cells. However, at 39
369 µg/ml, there was no antiviral activity from MβCD alone. We, therefore, combined 39
370 µg/ml MβCD with 10 µM UMB18 to investigate whether extracting cholesterol from cells
371 treated with UMB18 would reduce the antiviral activity. Fig. 6F demonstrates that
372 UMB18 is a potent inhibitor, reducing percentage infection by about 90% compared to
373 DMSO-treated control cells. When combined with MβCD, the percentage inhibition is
374 approximately 40%, demonstrating that MβCD significantly reduced the antiviral activity
375 of UMB18. These data demonstrate that reduced expression of the *Scap* or *Srebf* genes

376 or cholesterol extraction from cells significantly reduced the antiviral activity of UMB18,
377 pointing towards increased cholesterol being the antiviral mechanism of action for
378 UMB18.
379

380 # Discussion

381 We have identified the SKI complex as a potential host-directed antiviral drug target (1)
382 and determined that the novel compound, UMB18, specifically binds to its *in silico*
383 predicted target, SKIC8. RNA transcriptomics, validated by qRT-PCR, demonstrated
384 that UMB18 treatment caused significant upregulation of genes involved in the
385 mevalonate pathway, and this corresponded to an increase in total cellular cholesterol
386 (Fig. 1 and 2). Interestingly, these results were in the context of media supplemented
387 with fetal bovine serum which contains cholesterol that can inhibit activation of the
388 mevalonate pathway through a negative feedback loop. We found that cells cultured in
389 serum-free media activated the mevalonate pathway and UMB18 had minimal additive
390 effect (Fig. 3). We propose that UMB18 cannot further increase signaling to the already
391 active pathway. However, we cannot rule out alternative hypotheses that UMB18 may
392 be modified by components of serum, may not be effectively taken into cells in the
393 absence of serum or may have impacts on roles adjacent to the mevalonate pathway
394 such as protein prenylation. We do suspect some of these may have a role since virus
395 replication is attenuated in serum-free media but UMB18 still provides a greater level of
396 inhibition (Fig. 3D). As this compound is further developed, biochemical experiments to
397 look at the impact of serum on its activity will be performed.
398

399 With the observed increase in expression of mevalonate pathway genes we were drawn
400 to the SCAP/SREBP axis as the master regulators of sterol and fatty acid synthesis
401 (11). Depletion of any of *Scap, Srebf1*, or *Srebf2* by siRNA resulted in an attenuation of
402 UMB18-induced upregulation of mevalonate pathway genes, indicating that the UMB18
403 effect is through this canonical signaling pathway (Fig. 5). Crucially, the antiviral activity
404 of UMB18 against SARS-CoV-2 was markedly decreased when *Scap* or *Srebf* genes
405 were depleted from cells, arguing that the increased expression of mevalonate pathway
406 genes is essential for antiviral activity (Fig. 6). Consistently, extraction of cellular
407 cholesterol using MβCD also attenuated the antiviral activity of UMB18, reinforcing the
408 importance of increased cellular cholesterol in mediating antiviral activity (Fig. 6).
409
410 Our findings collectively reveal that UMB18 binds the SKI complex and activates
411 SREBP-mediated gene expression, leading to an increase in cellular cholesterol which
412 is crucial for antiviral efficacy of the compound. We have shown that UMB18 and similar
413 SKI-targeting compounds exhibit broad-spectrum activity against enveloped viruses,
414 including coronaviruses, orthomyxoviruses, and filoviruses (1), all of which rely on
415 manipulation of cellular membranes for efficient replication. We hypothesize that
416 UMB18-mediated increase in total cellular cholesterol, which causes an increase in
417 membrane rigidity, impedes the ability of these viruses to manipulate membranes and
418 thus disrupts efficient replication.
419
420 Previous studies have suggested SARS-CoV-2 infection may downregulate expression
421 of mevalonate pathway genes associated with cholesterol synthesis (18,19). It would

422 therefore be reasonable to hypothesize that increasing expression of these genes would
423 have antiviral activity, in alignment with our data. However, contrasting studies have
424 suggested that SARS-CoV-2 and other coronaviruses cause an increase in lipid
425 metabolism, mediated by the SREBPs (20–22), and that lowered cellular cholesterol
426 can be antiviral (23,24). We also present data from our MβCD studies that lowered
427 cellular cholesterol can be antiviral (Fig. 6E). Therefore, we propose that there may be a
428 delicate equilibrium in cholesterol levels, or a “Goldilocks” range of cellular cholesterol
429 necessary to support viral replication. Deviations from this balance, whether through
430 insufficient or excessive cholesterol, disrupts membrane dynamics and adversely affects
431 viral replication. At an organismal level, increased cholesterol usually comes from, or
432 with, various other underlying health conditions which can all impact viral disease
433 pathogenesis. In future work, we intend to further study the role these cellular
434 cholesterol changes have at an organismal level using animal models of UMB18
435 treatment.
436
437 One hypothesis for the mechanism through which UMB18 is causing the SREBP-
438 mediated transcriptional changes draws from work by Yang *et al.* (16), which linked
439 SKIC2 deletion in mice to an increase in mTORC1 signaling. Despite efforts to
440 investigate whether UMB18 activated mTORC1 as assessed by phosphorylation levels
441 of S6K1, we observed no significant changes (Fig. 4). The activation of mTORC1 drives
442 many cellular changes, one of which is the activation of the SREBP proteins, and thus a
443 link between the SKI complex and mTORC1 activation could make sense in the context

444 of our data. It is possible that UMB18 could activate mTORC1 but not at a level to
445 observe changes to the phosphorylation status of S6K1.
446
447 Alternatively, UMB18 may alter the activity the RNA helicase activity of the SKI complex
448 and impact genes that regulate SCAP/SREBP proteins independently of mTORC1. For
449 instance, the SKI complex has been shown to have a role in resolution of stalled
450 ribosomes (25) which we hypothesize to be disrupted by treatment with UMB18. Stalled
451 ribosomes can activate ZAKα, which can in turn activate JNK signaling (26) and JNK
452 signaling has been linked to activation of SREBPs (27). Future research will explore the
453 interaction between UMB18, the SKI complex and these various cellular signaling
454 pathways.
455
456 This study advances our understanding of our developmental host-directed, broad-
457 spectrum antiviral therapeutic targeting the SKI complex. Building on our previous work
458 which established the SKI complex as a host-directed target to inhibit diverse highly
459 pathogenic human viruses, we reveal a crucial role for increased cellular cholesterol in
460 mediating this antiviral effect. Our findings prompt further investigation into the
461 mechanisms by which the SKI complex, an RNA helicase associated with 3' to 5' RNA
462 degradation, influences metabolic pathways crucial for lipid and cholesterol synthesis, a
463 finding that will be the focus of future work.
464

465 Material and Methods

466 **Mammalian cell culture**

467 A549 cells and A549 cells overexpressing human ACE2 (A549-ACE2, kindly provided
468 by Dr. Brad Rosenberg (MSSM, NYC)) were cultured in DMEM (Quality Biologicals),
469 supplemented with 10% (v/v) heat inactivated fetal bovine serum (FBS; Sigma) and 1%
470 (v/v) penicillin/streptomycin (pen/strep, 10,000 U/ml / 10 mg/ml; Gemini Bio-Products).
471 VeroE6 cells overexpressing TMPRSS2 (VeroT, kindly provided by Shutoku Matsuyama
472 (National Institute of Infectious Diseases, Japan - Shirato2018_Virology) were cultured
473 in DMEM, supplemented with 10% FBS, 1% pen/strep and 1% (v/v) L-glutamine (2 mM
474 final concentration, Gibco). Cells were maintained at 37°C and 5% CO_2.
475

476 **Chemical compounds**

477 SKI targeting compounds were synthesized by, and purchased from, Dalriada Drug
478 Discovery and were previously described (1). Methyl-beta-cyclodextrin (MβCD) was
479 purchased from Sigma.
480

481 **Viruses and infections**

482 Details on stock production have been described previously (1). SARS-CoV-2 strain
483 Washington 1 (WA1) was initially provided by the CDC (BEI #NR-52281). All
484 coronavirus work was performed in a Biosafety Level 3 laboratory and approved by our
485 Institutional Biosafety Committee. In all cases of infection for experiments, cells were
486 plated one day prior to infection to be at a desired confluence for infection. All viral titer
487 were determined using plaque assays on VeroT cells as described (28). For
488 experimental infections, virus was diluted to indicated MOI in media used for culture of

489 A549 cells with addition of chemical compounds or controls as appropriate. For
490 experiments using MβCD, 50 mM Hepes (Gibco) was additionally added to the media.
491

492 **RNA extraction and qRT-PCR**

493 RNA extractions and cDNA reactions were performed as described previously (1) using
494 Direct-zol RNA miniprep kit (Zymo Research) and RevertAid RT Kit (Thermo Scientific).
495 The primers used are listed in the table below. A QuantStudio 5 (Applied Biosystems)
496 was used for the qRT-PCR reactions. Loading was normalized using GAPDH and fold
497 change was determined by calculating ΔΔCT after normalization.

498 RT-PCR primers

499 All primers for qRT-PCR were purchased from Integrated DNA Technologies (IDT) using
500 their pre-designed qPCR assay primers:

Gene target	IDT Assay ID
SKIC2 (A.K.A SKIV2L)	Hs.PT.58.14722008
SKIC3 (A.K.A TTC37)	Hs.PT.58.26762302
SKIC8 (A.K.A WDR61)	Hs.PT.58.157001
HMGCS1	Hs.PT.58.4084870
HMGCR	Hs.PT.58.41105491
MVK	Hs.PT.58.40379926
MVD	Hs.PT.58.39035173
IDI1	Hs.PT.58.1930362
FDPS	Hs.PT.58.27570524
MSMO1	Hs.PT.58.3747602
SCAP	Hs.PT.58.45442299
SREBF1	Hs.PT.58.3359761

SREBF2	Hs.PT.58.45335433
GAPDH	Hs.PT.39a.22214836

501

502

503 **Transcriptomic sequencing and analysis**

504 Library preparation and sequencing were carried out by the University of Maryland
505 Institute of Genomic Sciences (IGS; Baltimore, MD, USA) on an Illumina NovaSeq
506 6000; 100bp paired-end sequencing on an S4 flow cell (Illumina, San Diego, CA, USA).
507 Reads were preprocessed using cutadapt v3.4(29), then aligned to the *Homo sapiens*
508 genome with STAR v2.7.8(30). Gene expression analysis was carried out using
509 DESeq2 v4.1.0(31) in R (Rstudio, Boston, MA, USA). Pathway analysis was carried out
510 using Ingenuity Pathway Analysis (QIAGEN, Hilden, Germany) using an alpha value of
511 $p_{adj} < 0.01$ to call a gene significantly differentially expressed. Raw sequence data is
512 available in the NCBI Sequence Read Archive under the accession number
513 PRJNA1055076.

514

515 **Mass spectrometry imaging**

516 A modified cell culture apparatus was used for compatibility with mass spectrometry
517 imaging (MSI). Briefly, Superfrost plus gold microscope slides were autoclaved with
518 flexible silicon 12-well transwell adapters (Flexiperm, Starstedt), dried completely, and
519 the transwell adapters mounted. Wells were coated with 0.1 mg/mL poly-l-lysine (0.1 M
520 borate buffer pH 8.5) overnight at 37°C, aspirated, and dried. Cells were grown in the
521 transwells overnight and subsequently treated with 10 μM UMB18 or 0.1% DMSO for
522 24h. At the end of the incubation, supernatants were aspirated, the transwell mount was

523 removed, and the slides were submerged in ice-cold 50 mM ammonium formate (pH
524 6.7) for 1 minute with gentle rocking. Excess buffer was removed by tilting and using
525 absorbent paper. Slides were dried, flat, in a desiccator for 20 minutes. Silver-assisted
526 laser desorption ionization (Ag-LDI) was used to ionize cholesterol on a quadropole time
527 of flight (qTOF) mass spectrometer in imaging mode (Yang2020_JMassSpectrom).
528 Silver nitrate (8.5 mg/mL in 0.1% trifluoroacetic acid/methanol) was sprayed on the
529 slides using an HTX M5 Matrix Sprayer with the following settings: 45°C nozzle, 40 mm
530 height, 24 passes, 0.075 mL/min flow, 500 mm/min speed, 4 mm track spacing, 20 psi,
531 2 L/min N2, in "CC" pattern, with 0 s dry time between passes. Cholesterol imaging data
532 were captured from an area of uniform monolayer (>80% confluence) integrity guided by
533 an optical pre-scan using a Bruker Daltonics timsTOF Flex (Billerica, MA) in positive ion
534 mode with a 50 μM scan area (11 μM x 11 μM beamscan), over range *m/z* 100-1000
535 with enhanced quadratic fit calibration to Agilent Tune-Mix, 500 shots per pixel at 10 kHz
536 with 5-point setting in M5 small laser focus. Total scan area per sample was ~3 mm^2
537 resulting in ~1200 pixels per replicate, with quadruplicate samples per condition. Data
538 analyzed in SCiLS Lab (Bruker Daltonics), normalized (total ion current), projected with
539 hotspotting on, and visualized as the ion *m/z* 493.260 +/-2.2 mDa ($[cholesterol+Ag_{107}]^+$)
540 ion; the $[cholesterol+Ag_{109}]^+$ ion data agreed. Student's T-test and a receiver-operator
541 characteristic were performed between vehicle-treated and UMB18-treated cells on
542 quadruplicate samples.
543
544 **Expression and purification of SKIC8**

545 Transformed *E. coli* BL21 (DE3) cells containing the full-length human *SKIC8* gene with
546 a HisX6 tag in the pET-28a(+) vector were grown in Luria-Bertani (LB)-Kanamycin broth
547 at 37ºC until the optical density at 600 nm equaled 0.8. SKIC8 protein expression was
548 induced with 1 mM Isopropyl β-D-1-thiogalactopyranoside for 20 h at 15°C. Cells were
549 lysed using Bugbuster (Novagen) supplemented with protease and phosphatase
550 inhibitors (Thermo Scientific). Lysates were clarified by centrifugation at 14,000 rpm for
551 30 min. and the supernatant was applied to a Talon Metal Affinity Resin (Clontech)
552 column equilibrated in 50 mM sodium phosphate (pH 7.8) containing 10 mM imidazole
553 and 300 mM NaCl. The column was washed with the same sodium phosphate buffer
554 containing 20 mM imidazole. SKIC8 was eluted in 50 mM sodium phosphate (pH 7.8)
555 containing a 50-250 mM imidazole gradient and 300 mM NaCl. The fractions containing
556 SKIC8, as determined following SDS-PAGE, were pooled, and concentrated with an
557 Amicon ultrafiltration cell (Millipore, Bedford, MA). The concentrated protein was
558 dialyzed against 20 mM Tris-HCl (pH 7.8) containing 150 mM NaCl.
559
560 **Surface Plasmon Resonance (SPR)**
561 SKIC8 and test compound interactions were evaluated using a Biacore T-200
562 instrument (GE Healthcare). A carboxymethylated dextran chip (CM5, GE Healthcare)
563 was used to immobilize SKIC8. A net positive charge is required for direct amine
564 coupling; therefore, the proteins were diluted to a final concentration of 30 µg/ml in 10
565 mM sodium acetate buffer pH 4.0. The protein was injected at 2 µl/min until
566 approximately a 4500 resonance/response unit level of immobilized SKIC8 was
567 reached, and then the flow cell was deactivated with 1 M ethanolamine HCl (pH 8.5).

568 Degassed 20 mM Hepes (pH 7.4) containing 5 mM MgCl2, 100 mM NaCl, and 0.005%
569 Nonidet P40 was utilized as continuous running buffer for all experiments. Test
570 compound binding interactions with SKIC8 were investigated by injecting test compound
571 (1.0 –50 μM) at a flow rate of 20 μl/min. The resulting sensorgrams were analyzed using
572 BIAevaluation 3.1 software (GE Healthcare) to determine the dissociation constant (K_D)
573 as previously described(32).
574
575 **RNAi knockdown**
576 Cells were seeded to 24-well plates at a density of 4.4e4 cells/well one day prior to
577 transfection. Transfections were performed using Oligofectamine (Thermo Scientific) to
578 the manufacture's methods. Briefly, per well of transfection, 4.4μl Opti-MEM (Gibco) was
579 mixed with 2.2μl Oligofectamine and incubated at room temperature (RT°C) for 5 min,
580 while 35.5μl Opti-MEM was mixed with 0.8μl 50mM siRNA in a separate tube. The two
581 tubes were combined and incubated at RT°C for 20 minutes prior to addition of 177μl
582 Opti-MEM. Cells were washed 1x with PBS and 1x with OptiMEM then 200μl of
583 transfection mixture was added per well. All siRNAs were purchased from Sigma using
584 their Rosetta prediction system for predesigned sequences. MISSION siRNA Universal
585 Negative Control #1 (Sigma) was used as the scrambled control sequence. Sequences
586 are displayed in table:
587 RNAi sequences

Gene name	**siRNA ID**
SKIC2 (A.K.A SKIV2L)	SASI_Hs01_00196881
SKIC3 (A.K.A TTC37)	SASI_Hs01_00010354

SKIC8 (A.K.A WDR61)	SASI_Hs01_00155941
SCAP si-1	SASI_Hs01_00032110
SCAP si-2	SASI_Hs01_00032111
SREBF1 si-1	SASI_Hs01_00051828
SREBF1 si-2	SASI_Hs01_00051829
SREBF2 si-1	SASI_Hs01_00075424
SREBF2 si-2	SASI_Hs01_00075425
SREBF2 si-3	SASI_Hs01_00075426

588

589 **Western blotting**

590 Whole cell lysates were made using Triton-X100 (Tx100) lysis buffer lysis buffer (1%
591 Tx100 (v/v), 150mM NaCl, 50mM Tris (all Sigma), pH8). In all cases 1x cOmplete Mini,
592 EDTA-Free protease inhibitor cocktail (Roche) was added to the lysis buffer and for
593 experiments involving S6K and phospho-S6K (pS6K), Phosphatase Inhibitor Cocktail 2
594 (Sigma) was additionally used. Western blotting procedures have been previously
595 described(33). Primary antibodies used as follows: p70 S6K (Cell Signaling
596 Technologies #9202S, 1:1000 dilution), phospho-p70 S6K (T421/S424) (Cell Signaling
597 Technologies #9204S, 1:1000 dilution) and mouse anti-tubulin (clone DMA1A, Sigma,
598 1:1000). Secondary antibodies were used as follows: goat anti-rabbit HRP and goat
599 anti-mouse HRP (both 0.8 mg/ml, Thermo Scientific, 1:10,000 diluted) which were
600 detected using ECL Prime (Amersham).

601

602 **Data analysis**

All graphs produced and statistical analysis performed using GraphPad Prism 10.5 software.

Acknowledgements

Acknowledgments: We would like to thank all of the Frieman, Jackson and Coughlan lab members for their help in this study.

Funding: MBF is supported by an endowment from The Alicia and Yaya Foundation. The funders had no role in study design, data collection and analysis, decision to publish, or preparation of the manuscript.

References

1. Weston S, Baracco L, Keller C, Matthews K, McGrath ME, Logue J, et al. The SKI complex is a broad-spectrum, host-directed antiviral drug target for coronaviruses, influenza, and filoviruses. Proc Natl Acad Sci U S A. 2020 Dec 1;117(48):30687–98.
2. Houseley J, Tollervey D. The Many Pathways of RNA Degradation. Cell. 2009 Feb 20;136(4):763–76.
3. Schneider C, Tollervey D. Looking into the barrel of the RNA exosome. Nat Struct Mol Biol. 2014 Jan;21(1):17–8.
4. Januszyk K, Lima CD. The eukaryotic RNA exosome. Curr Opin Struct Biol. 2014 Feb;24:132–40.
5. Johnson SJ, Jackson RN. Ski2-like RNA helicase structures: common themes and complex assemblies. RNA Biol. 2013 Jan;10(1):33–43.
6. Toh-E A, Guerry P, Wickner RB. Chromosomal superkiller mutants of Saccharomyces cerevisiae. J Bacteriol. 1978 Dec;136(3):1002–7.

627 7. Widner WR, Wickner RB. Evidence that the SKI antiviral system of Saccharomyces
628 cerevisiae acts by blocking expression of viral mRNA. Mol Cell Biol. 1993
629 July;13(7):4331–41.

630 8. Goldstein JL, Brown MS. Regulation of the mevalonate pathway. Nature. 1990
631 Feb;343(6257):425–30.

632 9. Luo J, Yang H, Song BL. Mechanisms and regulation of cholesterol homeostasis.
633 Nat Rev Mol Cell Biol. 2020 Apr;21(4):225–45.

634 10. Cerqueira NMFSA, Oliveira EF, Gesto DS, Santos-Martins D, Moreira C, Moorthy
635 HN, et al. Cholesterol Biosynthesis: A Mechanistic Overview. Biochemistry. 2016
636 Oct 4;55(39):5483–506.

637 11. Brown MS, Goldstein JL. The SREBP Pathway: Regulation of Cholesterol
638 Metabolism by Proteolysis of a Membrane-Bound Transcription Factor. Cell. 1997
639 May 2;89(3):331–40.

640 12. Hua X, Nohturfft A, Goldstein JL, Brown MS. Sterol resistance in CHO cells traced to
641 point mutation in SREBP cleavage-activating protein. Cell. 1996 Nov 1;87(3):415–
642 26.

643 13. Shimomura I, Shimano H, Horton JD, Goldstein JL, Brown MS. Differential
644 expression of exons 1a and 1c in mRNAs for sterol regulatory element binding
645 protein-1 in human and mouse organs and cultured cells. Journal of Clinical
646 Investigation. 1997 Mar 3;99(5):838.

647 14. Nohturfft A, DeBose-Boyd RA, Scheek S, Goldstein JL, Brown MS. Sterols regulate
648 cycling of SREBP cleavage-activating protein (SCAP) between endoplasmic
649 reticulum and Golgi. Proceedings of the National Academy of Sciences. 1999 Sept
650 28;96(20):11235–40.

651 15. Sun LP, Li L, Goldstein JL, Brown MS. Insig required for sterol-mediated inhibition of
652 Scap/SREBP binding to COPII proteins in vitro. J Biol Chem. 2005 July
653 15;280(28):26483–90.

654 16. Yang K, Han J, Asada M, Gill JG, Park JY, Sathe MN, et al. Cytoplasmic RNA
655 quality control failure engages mTORC1-mediated autoinflammatory disease.
656 Journal of Clinical Investigation. 2022 Jan 18;132(2):e146176.

657 17. Horton JD, Goldstein JL, Brown MS. SREBPs: activators of the complete program of
658 cholesterol and fatty acid synthesis in the liver. J Clin Invest. 2002 May
659 1;109(9):1125–31.

660 18. Gomez Marti JL, Wells A, Brufsky AM. Dysregulation of the mevalonate pathway
661 during SARS-CoV-2 infection: An in silico study. Journal of Medical Virology.
662 2021;93(4):2396–405.

663 19. Wang X, Zhao Y, Yan F, Wang T, Sun W, Feng N, et al. Viral and Host
664 Transcriptomes in SARS-CoV-2-Infected Human Lung Cells. J Virol. 2021 Aug
665 25;95(18):e0060021.

666 20. Dias SSG, Soares VC, Ferreira AC, Sacramento CQ, Fintelman-Rodrigues N,
667 Temerozo JR, et al. Lipid droplets fuel SARS-CoV-2 replication and production of
668 inflammatory mediators. PLOS Pathogens. 2020 Dec 16;16(12):e1009127.

669 21. Gao P, Ji M, Liu X, Chen X, Liu H, Li S, et al. Apolipoprotein E mediates cell
670 resistance to influenza virus infection. Science Advances. 2022 Sept
671 21;8(38):eabm6668.

672 22. Yuan S, Chu H, Chan JFW, Ye ZW, Wen L, Yan B, et al. SREBP-dependent
673 lipidomic reprogramming as a broad-spectrum antiviral target. Nat Commun. 2019
674 Jan 10;10(1):120.

675 23. Wing PAC, Schmidt NM, Peters R, Erdmann M, Brown R, Wang H, et al. An ACAT
676 inhibitor suppresses SARS-CoV-2 replication and boosts antiviral T cell activity.
677 PLOS Pathogens. 2023 May 3;19(5):e1011323.

678 24. Wang H, Yuan Z, Pavel MA, Jablonski SM, Jablonski J, Hobson R, et al. The role of
679 high cholesterol in SARS-CoV-2 infectivity. Journal of Biological Chemistry
680 [Internet]. 2023 June 1 [cited 2024 Aug 28];299(6). Available from:
681 https://www.jbc.org/article/S0021-9258(23)01791-X/abstract

682 25. Zinoviev A, Ayupov RK, Abaeva IS, Hellen CUT, Pestova TV. Extraction of mRNA
683 from Stalled Ribosomes by the Ski Complex. Molecular Cell. 2020 Mar
684 19;77(6):1340-1349.e6.

685 26. Snieckute G, Genzor AV, Vind AC, Ryder L, Stoneley M, Chamois S, et al.
686 Ribosome stalling is a signal for metabolic regulation by the ribotoxic stress
687 response. Cell Metabolism. 2022 Dec;34(12):2036-2046.e8.

688 27. Kotzka J, Knebel B, Haas J, Kremer L, Jacob S, Hartwig S, et al. Preventing
689 Phosphorylation of Sterol Regulatory Element-Binding Protein 1a by MAP-Kinases
690 Protects Mice from Fatty Liver and Visceral Obesity. PLOS ONE. 2012 Feb
691 27;7(2):e32609.

692 28. Weston S, Coleman CM, Haupt R, Logue J, Matthews K, Li Y, et al. Broad Anti-
693 coronavirus Activity of Food and Drug Administration-Approved Drugs against
694 SARS-CoV-2 In Vitro and SARS-CoV In Vivo. J Virol. 2020 Oct 14;94(21):e01218-
695 20.

696 29. Martin M. Cutadapt removes adapter sequences from high-throughput sequencing
697 reads. EMBnet.journal. 2011 May 2;17(1):10–2.

698 30. Dobin A, Davis CA, Schlesinger F, Drenkow J, Zaleski C, Jha S, et al. STAR:
699 ultrafast universal RNA-seq aligner. Bioinformatics. 2013 Jan 1;29(1):15–21.

31. Love MI, Huber W, Anders S. Moderated estimation of fold change and dispersion for RNA-seq data with DESeq2. Genome Biology. 2014 Dec 5;15(12):550.

32. Burkhard KA, Chen F, Shapiro P. Quantitative analysis of ERK2 interactions with substrate proteins: roles for kinase docking domains and activity in determining binding affinity. J Biol Chem. 2011 Jan 28;286(4):2477–85.

33. Weston S, Matthews KL, Lent R, Vlk A, Haupt R, Kingsbury T, et al. A Yeast Suppressor Screen Used To Identify Mammalian SIRT1 as a Proviral Factor for Middle East Respiratory Syndrome Coronavirus Replication. J Virol. 2019 Aug 15;93(16):e00197-19.

Author Contributions:

- Conceptualization: SW, MBF
- Data curation: LT,
- Formal analysis: SW, LT, AS, PS,
- Funding acquisition: MBF
- Investigation: SW, LB, AS, GK,
- Methodology: SW, LT, AS, PS,
- Resources: ADM
- Supervision: MBF
- Visualization: SW, LT, AS, PS,
- Writing – original draft: SW, AS, PS, MBF
- Writing – review & editing: SW, MFB

Competing Interests: The authors declare the following competing interesting: M.B.F is the lead inventor along with S.W. and A.D.M as contributing inventors for patents held for development of SKI targeting compounds (of which UMB18 is one) with

726 antiviral activity. The patent filings were through University of Maryland, Baltimore
727 and listed as PCT/US20/36483 and PCT/US2021/1061863. There has been a
728 corporate partnership with Aikido Pharmaceuticals for developmental research on
729 the compound along with others that target the SKI complex. This developmental
730 work has not influenced the academic research presented in this paper.

731 Patents: Filed patents: Patents on UMB18 and related compounds have been filed
732 through University of Maryland, Baltimore and listed as PCT/US20/36483 and
733 PCT/US2021/1061863.

734 Data and Material Availability: All data needed to evaluate the conclusions in this paper
735 are present in the paper and supplementary materials. Data are also deposited at
736 https://osf.io/63h8t/.

737

738 # Figure Legend

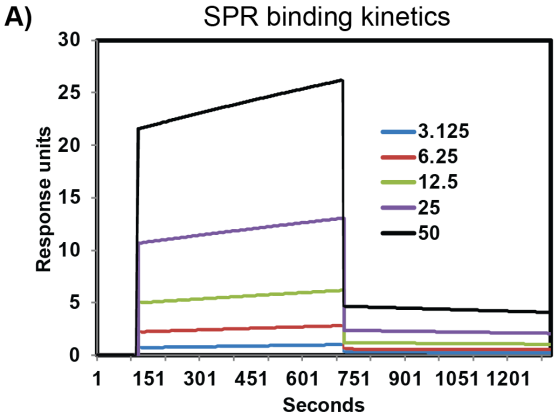

Conc (M)	RI (RU)
3.13E-06	0.7169
6.25E-06	2.224
1.25E-05	4.987
2.5E-05	10.68
5E-05	21.55

Conc (M)	KD (M)
3.13E-06	8.1E-05

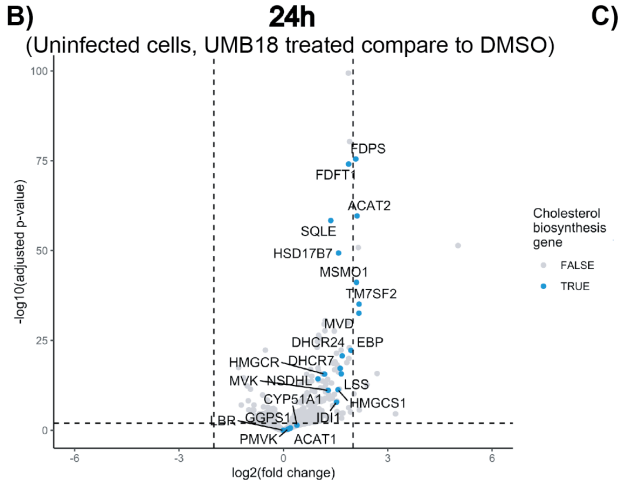

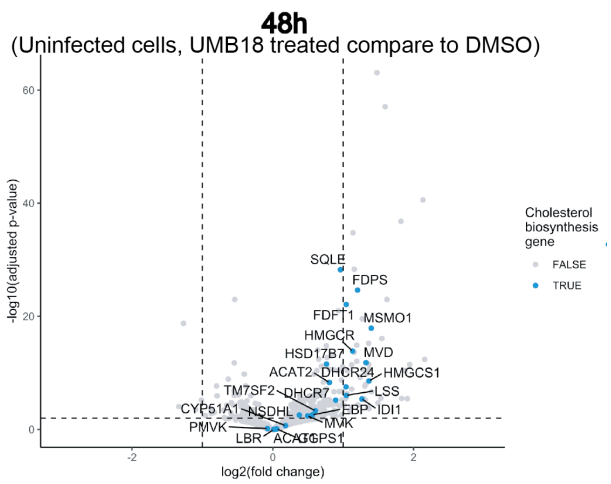

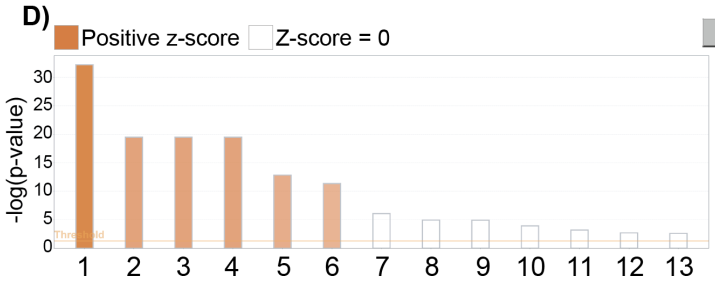

Column #	Pathway
1	Superpathway of Cholesterol Biosynthesis
2	Cholesterol Biosynthesis I
3	Cholesterol Biosynthesis II (via 24,25-dihydrolanosterol)
4	Cholesterol Biosynthesis III (via Desmosterol)
5	Superpathway of Geranylgeranyldiphosphate Biosynthesis I (via Mevalonate)
6	Mevalonate Pathway I
7	Zymosterol Biosynthesis
8	Oleate Biosynthesis II (Animals)
9	Epoxysqualene Biosynthesis
10	Trans, trans-farnesyl Diphosphate Biosynthesis
11	Ketogenesis
12	γ-linolenate Biosynthesis II (Animals)
13	Androgen Biosynthesis

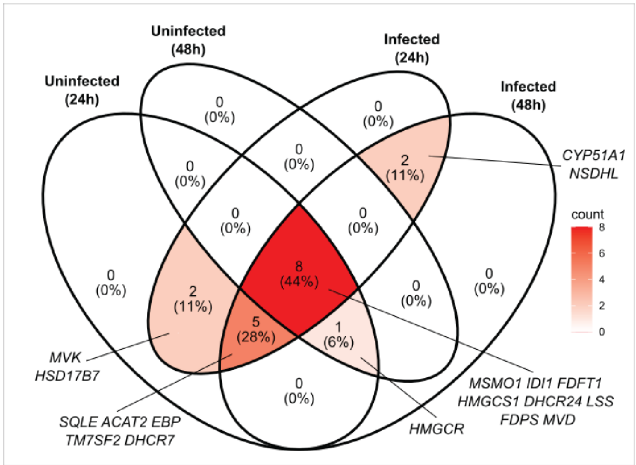

739

740 **Figure 1 – UMB18 directly binds SKIC8 and causes transcriptomic increases in**
741 **mevalonate pathway.**
742 A) Binding of UMB18 to SKIC8. The binding affinity of immobilized SKIC8 to UMB18 at
743 various concentrations was quantified by SPR as described in the methods. A KD of 81
744 μM was calculated for the binding. B) Volcano plots showing differential expression of
745 genes at 24h (top) and 48h (bottom) in uninfected A549-ACE2 cells treated with 10 μM
746 UMB18 compared to 0.1% DMSO treated, uninfected A549-ACE2 cells. Cholesterol
747 biosynthesis genes are colored blue and labeled. A horizontal dashed line is drawn at
748 $p_{adj} = 0.01$, vertical dashed lines are drawn at +/- 2-fold change. C) Plot showing
749 significantly enriched pathways in uninfected A549-ACE2 cells treated with UMB18
750 compared to DMSO treated, uninfected A549-ACE2 cells at 24h. Orange bars show
751 pathways with predicted increased pathway output ($z > 2$); white bars show pathways
752 with no predicted activity pattern ($z = 0$). D) Venn Diagram comparing upregulation of
753 cholesterol biosynthesis genes in UMB18-treated A549-ACE2 cells against timepoint-
754 and infection-matched, untreated controls. The number and color intensity in each area
755 corresponds to the number of cholesterol biosynthesis genes that are significantly
756 upregulated ($p_{adj} < 0.01$) and these genes are indicated.
757

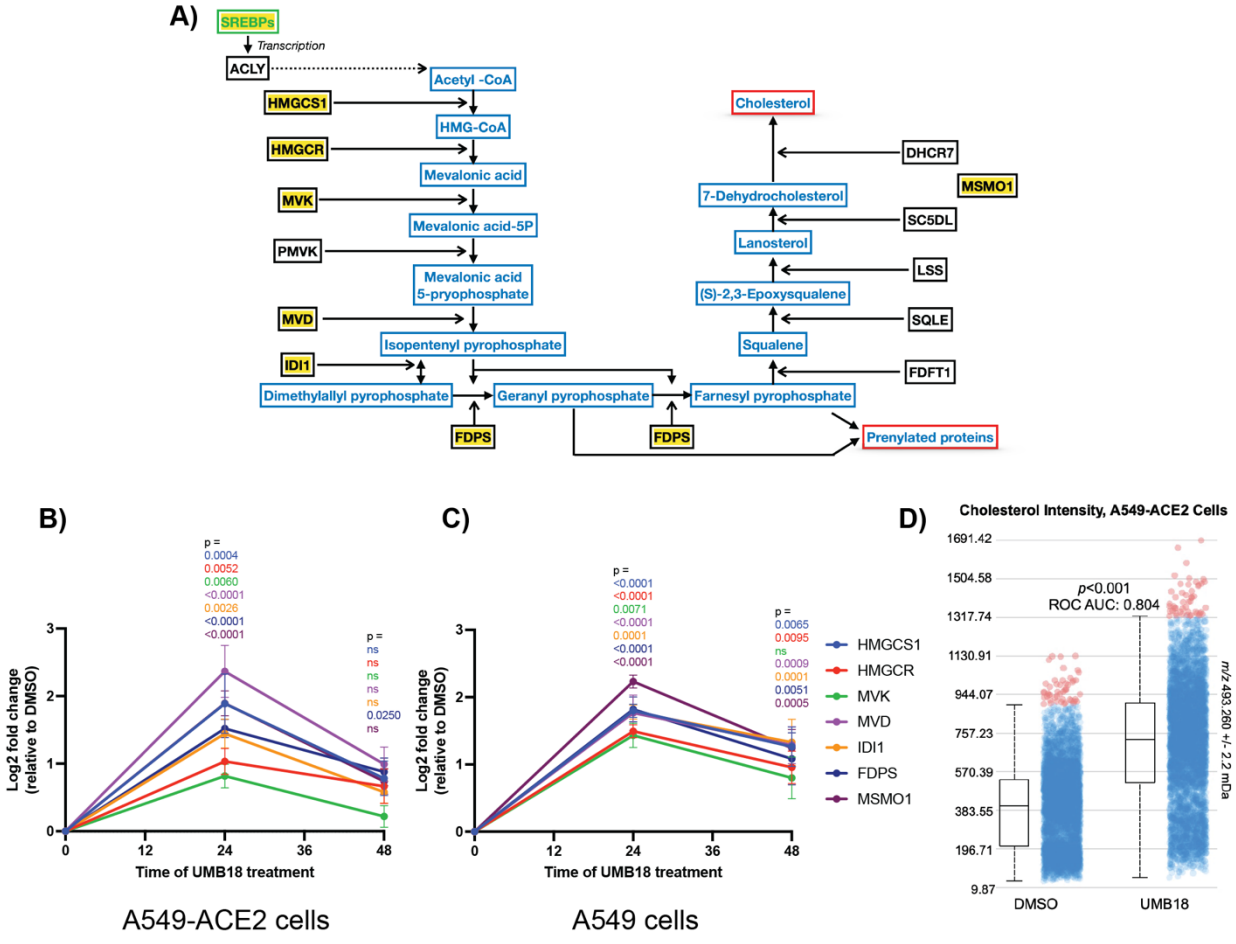

Figure 2 – UMB18 causes increased expression of mevalonate pathway genes and cellular cholesterol.

A) Simplified schematic representation of the mevalonate pathway leading to cholesterol synthesis. In blue are metabolic products of the pathway and in black are the enzymes that regulate the various steps with those that are highlighted being analyzed by qRT-PCR through the paper. B and C) A549-ACE2 cells (B) or A549 cells (C) were treated with 10 μM UMB18 or 0.1% DMSO vehicle control and collected at 24h or 48h in TRIzol for qRT-PCR analysis of expression of various genes throughout the mevalonate pathway. The Ct values were normalized to GAPDH as a housekeeping

769 gene control to calculate the ΔCt and then relative fold change calculated between
770 UMB18 treated cells and DMSO treated cells for the ΔΔCt. Plotted is the -ΔΔCt on a
771 Log2 scale to show relative fold change, plotting mean and standard error of the mean
772 as error bars. P values were calculated for the ΔCt values by two-way ANOVA with a
773 Tukey multiple comparison correction for each gene at the different time points and
774 treatments. Data are from 3 independent experiments each performed with triplicate
775 wells of treatment. D) Relative intensity cloud projection with box plot of *m/z* 493.260 +/-
776 2.2 mDa ([cholesterol+Ag_{107}]$^{+}$) ion per image pixel for UMB18- and DMSO-treated cells
777 with area-under-the-curve (AOC) from a receiver-operator characteristic analysis.
778 Student's T-test base on quadruplicate samples.
779

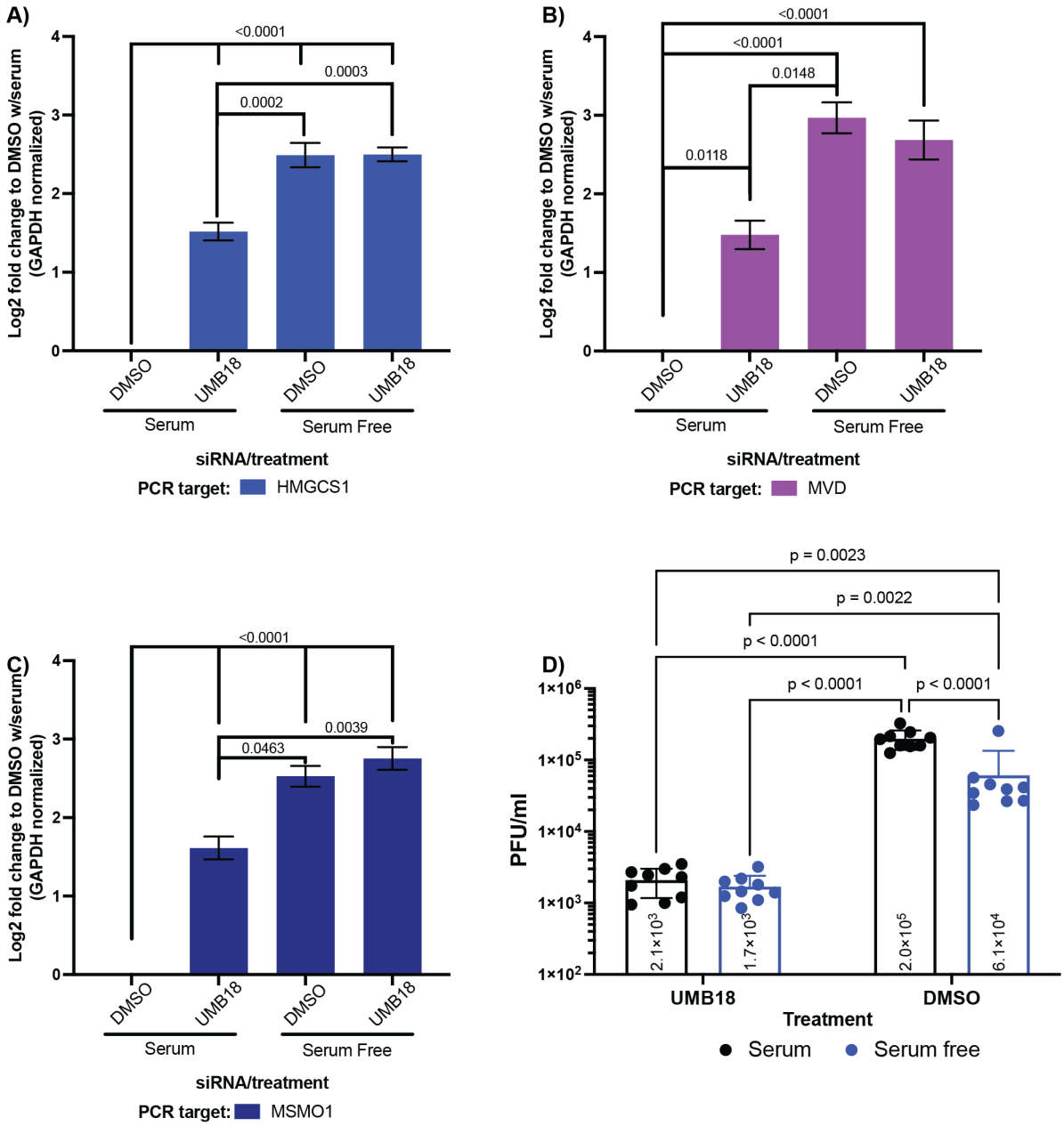

Figure 3 – UMB18 increases cellular cholesterol and exerts antiviral activity in serum containing media

A-C) A549-ACE2 cells were treated with 10 μM UMB18 or 0.1% DMSO in culture media containing 10% (v/v) fetal bovine serum (as described in Materials & Methods) or without supplemental serum (serum free). After 24h of treatment, cells were collected in TRIzol for qRT-PCR analysis of the three indicated genes (HMGCS1, MVD and

787 MSMO1, A-C). Analysis was performed, and data plotted as described in Figure 2. D)
788 A549-ACE2 cells were infected with SARS-CoV-2 at MOI 0.5 in serum containing or
789 serum free media with 10 μM UMB18 or 0.1% DMSO. 24-hour post-infection
790 supernatant was collected and used to titer virus by plaque assay on VeroTMPRSS2
791 cells. Plotted is the mean pfu/ml value from 3 independent experiments performed in
792 triplicate wells, with that value being displayed within each bar. Significance calculated
793 by two-way ANOVA with a Tukey multiple comparison correction. Only statically
794 significant ($p < 0.05$) comparisons are shown on the graph.
795

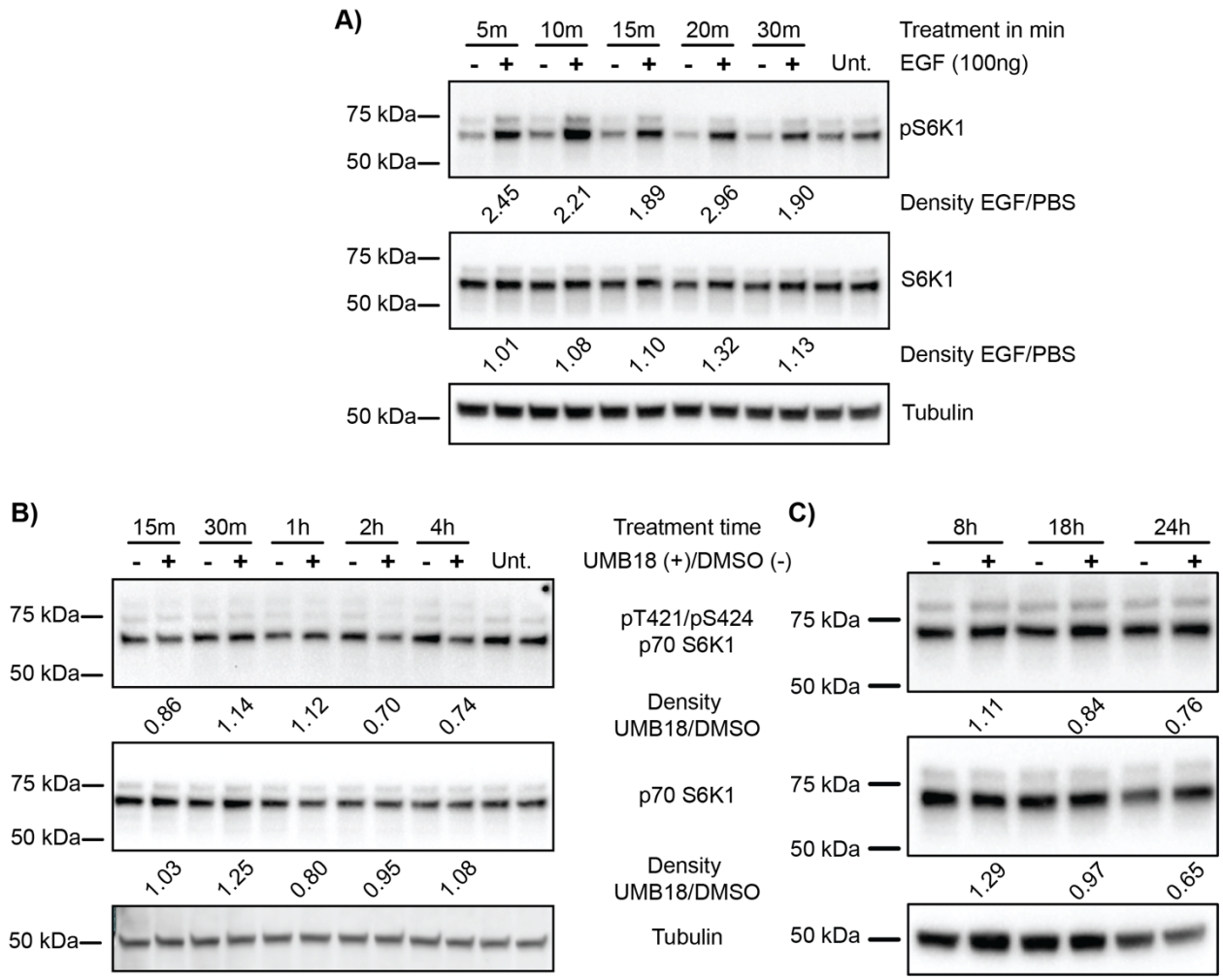

Figure 4 – UMB18 does not appear to activate mTOR signaling as assessed by phospho-S6K1.

A) A549-ACE2 cells were plated to plastic and the following day treated with 100 ng recombinant EGF, or PBS carrier alone. At time points between 5 and 30 min, cells were collected in Triton-X100 lysis buffer and prepared for western blotting (see Materials and Methods). Samples were separated on gels and blotted for phospho-S6K1 or S6K1 and tubulin was used as a loading control. All probes were detected with HRP. Density of bands was determined and quantified by setting relative to tubulin control and then reported as a relative band density of EGF treated compared to PBS treated at each

806 time point. B and C) A549-ACE2 cell were plated to plastic and the following day treated
807 with 10 μM UMB18 or 0.1% DMSO for the indicated time points or left untreated (for 4
808 hours in B). At each timepoint, cells were collected, and western blots run similarly to A.
809 All gels were imaged with HRP, except tubulin in B which was visualized by AlexaFluor
810 488. Density of UMB18 compared to DMSO at each time point is reported as in A.
811
812

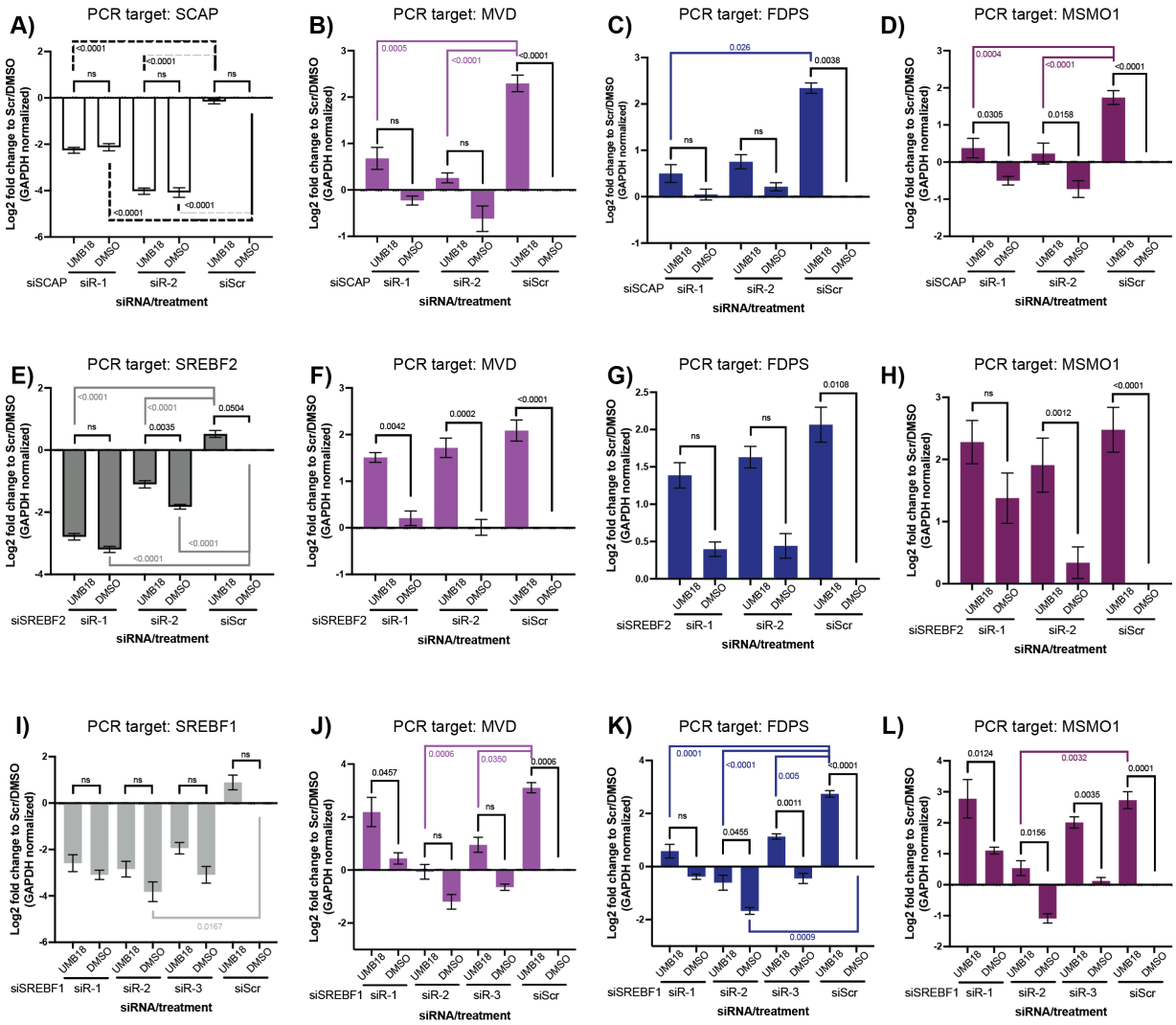

Figure 5 – UMB18 requires SCAP and SREBP genes to increase mevalonate pathway gene expression.

A549-ACE2 cells were transfected with unique siRNA sequences targeting *Scap* (A-D), *Srebf2* (E-H) or *Srebf1* (I-L) for 72h. The cells were then treated with 10 μM UMB18 or 0.1% DMSO for 24h and collected in TRIzol for qRT-PCR targeting the specified genes (the siRNA targeted genes or MVD, FDPS or MSMO1 as representatives of the mevalonate pathway). The Ct values were normalized to GAPDH as a housekeeping gene to determine the ΔCt and then relative fold change was calculated compared to

822 scrambled siRNA (siScr) transfected cells treated with DMSO (siScr/DMSO) for each of
823 the conditions for the ΔΔCt. The mean -ΔΔCt is plotted on a Log2 scale to show relative
824 fold change, plotting mean and standard error of the mean as error bars. P values were
825 calculated for the ΔCt values by two-way ANOVA with a Tukey multiple comparison
826 correction for each gene. Values were calculated comparing the mean within each
827 siRNA condition (UMB18 vs DMSO), displayed with black bars or within each treatment
828 condition where gene specific knockdown siRNA was compared to siScr for UMB18
829 treatment (color bars above graph) or DMSO treatment (color bars below graph). For
830 this later comparison, only statistically significant p values (< 0.05) are displayed. Data
831 are from 3 independent experiments each performed with triplicate wells of treatment.

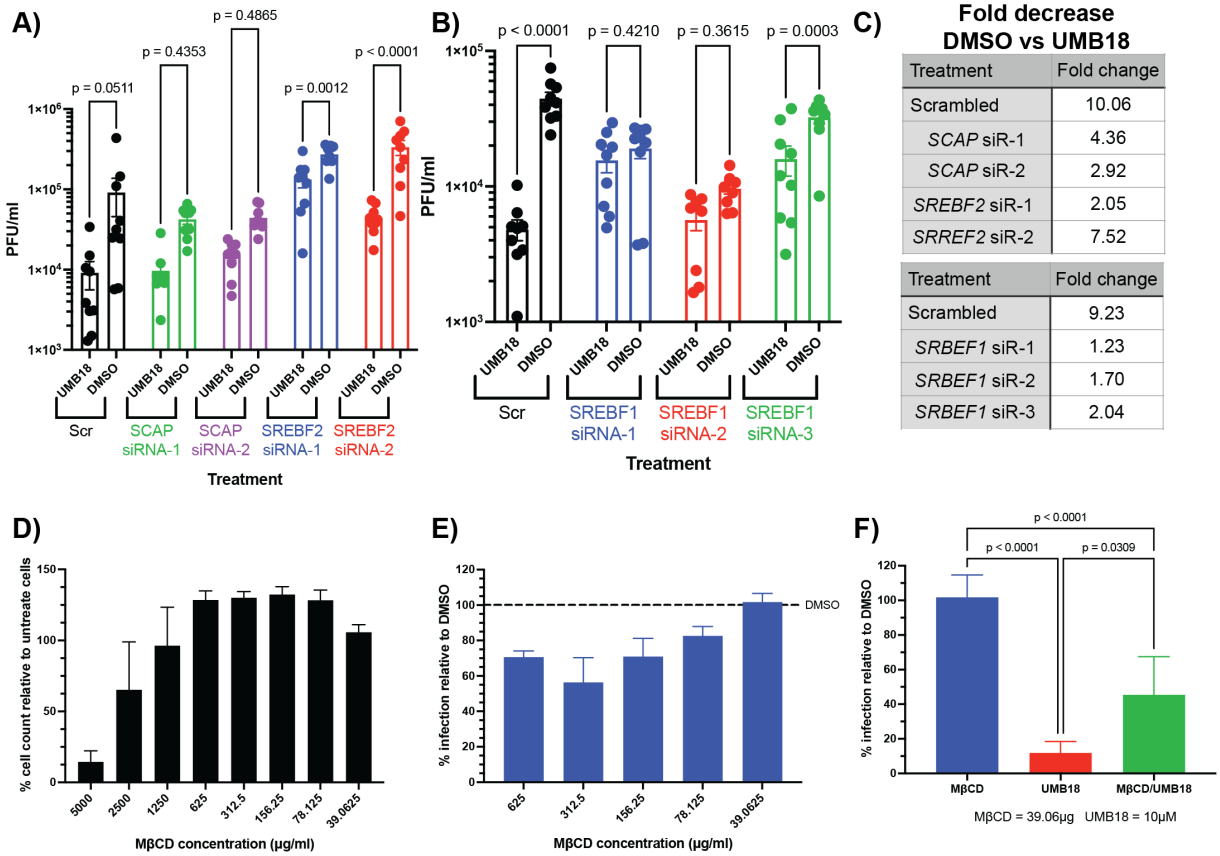

Treatment	Fold change
Scrambled	10.06
SCAP siR-1	4.36
SCAP siR-2	2.92
SREBF2 siR-1	2.05
SRREF2 siR-2	7.52

Treatment	Fold change
Scrambled	9.23
SRBEF1 siR-1	1.23
SRBEF1 siR-2	1.70
SRBEF1 siR-3	2.04

Figure 6 – Increased cellular cholesterol is required for UMB18-mediated antiviral activity.

A and B) A549-ACE2 cells were transfected with siRNA sequences targeting *Scap or Srebf2 or Srebf1* (sequences as used in Figure 5, *Scap* and *Srebf2* [A] transfections were experimentally performed together while *Srebf1* [B] were performed separately). Following transfection, cells were infected with SARS-CoV-2 at MOI 0.1 and treated with 10 µM UMB18 or 0.1% DMSO for 24h. Supernatant was collected from the cells and viral titer determined by plaque assay on VeroTMPRSS2 cells. The titer is plotted as plaque forming units/ml from each of the different transfection and treatment conditions. Using scrambled siRNA (siScr) as the control. Two-way ANOVA analysis was performed, and the p-values are plotted. Data are from three independent experiments

844 performed in triplicate. C) Fold change between titer of DMSO treated and UMB18
845 treated in each transfection condition summarized in a table format. D) A549-ACE2 cells
846 were treated with the indicated concentrations of methyl-beta-cyclodextrin (MβCD) for
847 24h prior to fixation with neutral buffered formalin. Cells were stained with Hoechst to
848 label nuclei and cell count per well (96 well format) was quantified with a Celigo high
849 content imager. Reported is the percentage total cell count compared to untreated cells
850 as a measure of cytotoxicity from MβCD treatment. E) A549-ACE2 cells were infected
851 with SARS-CoV-2 at MOI 3 and treated with the indicated concentrations of MβCD for
852 24h. Cells were similarly fixed with neutral buffered formalin then immunofluorescence
853 labeled for SARS-CoV-2 N protein and stained with Hoechst. High content imaging was
854 used to quantify percentage infection, and the plotted data are relative parentage
855 infection compared to untreated control cells. F) As in E, cells were infected with SARS-
856 CoV-2 at MOI 3 and treated with or without MβCD with either 10 μM UMB18 or 0.1%
857 DMSO. Cells were similarly fixed and labeled for high content imaging of percentage
858 infection. Plotted are the relative infection percentage to 0.1% DMSO treated cells for
859 each of the different conditions. An unpaired t-test was performed for each condition
860 and the p-values are reported. Data are from three independent experiments.